



Hydrogen generation from water splitting over polyfunctional perovskite oxygen carriers by using coke oven gas as reducing agent

Yanhui Long^{a,b,c}, Kun Yang^b, Zhenhua Gu^d, Shen Lin^b, Danyang Li^b, Xing Zhu^{a,b}, Hua Wang^a, Kongzhai Li^{a,b,*}

^a State Key Laboratory of Complex Nonferrous Metal Resources Clean Utilization, Kunming University of Science and Technology, Kunming 650093, Yunnan, China

^b Faculty of Metallurgical and Energy Engineering, Kunming University of Science and Technology, Kunming 650093, Yunnan, China

^c College of Energy Engineering, ZJU-UIUC, Zhejiang University, Hangzhou 310027, Zhejiang, China

^d School of Energy and Environment Science, Yunnan Normal University, Kunming 650500, Yunnan, China

ARTICLE INFO

Keywords:

Coke oven gas
Syngas
Hydrogen
Chemical looping
Ni-doped LaFeO₃

ABSTRACT

Via redox chemistry, chemical looping water splitting driven by the reduction of coke oven gas (COG) over an oxygen carrier was proposed to co-produce pure H₂ and H₂-rich syngas without a separation step. We designed an efficient LaFeO₃-based perovskite oxygen carriers by doping a small amount of Ni for preferentially oxidizing methane to syngas in the presence of CO and H₂ at relatively low temperatures (700–800 °C), which further improves the H₂ yield via water splitting. Compared with pure LaFeO₃, the methane conversion and syngas yield for LaNi_{0.07}Fe_{0.93}O_{3-λ} increase from 49.4% and 8.55 mol·kg⁻¹ to 98.6% and 12.58 mol·kg⁻¹ in the COG conversion step at 800 °C, respectively, and the H₂ yield rises from 1.91 mol·kg⁻¹ to 3.30 mol·kg⁻¹ in the water splitting step. Results from combined experimental characterizations and density functional theory (DFT) calculation reveal that the incorporation of Ni cations into LaFeO₃ lattice can greatly weaken the Fe-O bond and increase the lattice oxygen mobility, and the exsolved surface Ni species during the early stage of the reduction promote the activation of methane for further conversion. This contributes to the enhanced activity and lowered reaction temperature for syngas and H₂ generation. The LaNi_{0.07}Fe_{0.93}O_{3-λ} oxygen carriers also shows high stability in either reaction performance or material structure aspect during the successive redox cycles. This work demonstrates that it is feasible to design a high-performance oxygen carrier to preferentially convert methane in COG into syngas and further produce pure hydrogen via water splitting by using a chemical looping concept.

1. Introduction

Hydrogen has been regarded as one of the most promising future fuels, because “hydrogen economy” may be a long-term solution to the increasing worldwide energy demands and global climate change [1–4]. Nowadays, hydrogen is mainly produced from reforming of fossil fuels (e.g., nature gas and coal) with water, which is efficient but inevitably shows low CO₂ mitigation benefit. Alternatively, as one of the most important by-products in industrial sectors, coke oven gas (COG) with high contents of H₂ and CH₄ has been considered as an ideal gas for preparing high-purity hydrogen.

Coke oven gas is a rich and cheap secondary energy, which consists of H₂ (55–60 vol%), CH₄ (23–27 vol%), CO (5–8 vol%), CO₂ (less than 3 vol%) and trace H₂S. [5,6]. In 2019, 197.9 billion Nm³ COG was emitted

from the production of 47.1 million tons coke in China. Generally, COG can be used as fuel for heating or power generation in steel plants. However, only 20% of the produced COG is utilized, and excess COG even burns or is discharged into the atmosphere directly, resulting in huge waste of energy and serious environmental pollution [7]. In recent years, the conversion of COG to high value-added products (e.g., H₂ and syngas) has attracted widespread attention [8–12].

At present, pressure swing adsorption (PSA) [9], partial oxidation method [12,13], CO₂/steam reforming method [11,14,15] and membrane separation [16–18] are the most concerned technologies for COG utilization. However, PSA and partial oxidation method fail to directly produce pure H₂, and an additional separation process is therefore needed. The high cost of pure oxygen and the explosion risk of contact between O₂ and COG at high temperature also restrict the industrial

* Corresponding author at: State Key Laboratory of Complex Nonferrous Metal Resources Clean Utilization, Kunming University of Science and Technology, Kunming 650093, Yunnan, China.

E-mail addresses: kongzhai.li@foxmail.com, kongzhai.li@aliyun.com (K. Li).

<https://doi.org/10.1016/j.apcatb.2021.120778>

Received 25 June 2021; Received in revised form 22 September 2021; Accepted 27 September 2021

Available online 6 October 2021

0926-3373/© 2021 Elsevier B.V. All rights reserved.

production of POM [12]. For the membrane separation technology, it is extremely demanding on the reaction temperature ($> 1000\text{ }^{\circ}\text{C}$), and the preparation of membrane reactor is highly sophisticated [18]. Most importantly, it should be emphasized that all the above technologies (PSA, partial oxidation, CO_2 /steam reforming) need to undergo complete desulfurization pretreatment at relatively low temperatures because of the toxic effects of impurities (such as H_2S and tar) in the process of hydrogen production from coke oven gas [6].

Water splitting via a chemical looping concept driven by the reduction of methane or other fuels on an oxide redox catalyst (called oxygen carrier) is a novel technology for coproduction of pure hydrogen and syngas [19–22]. For example, methane can be selectively oxidized to CO and H_2 by a suitable oxygen carrier, and then water splitting occurs on the reduced catalyst to directly generate pure hydrogen and recover the catalyst [21,23]. When using the mixture of H_2 and CO as fuel, H_2 and CO can be oxidized by oxygen carriers to CO_2 and H_2O on one-half cycle, and pure hydrogen would be generated via water splitting step on the other half cycle [23–25]. In this case, the COG rich in H_2 , CH_4 and CO is regarded as an ideal fuel for chemical looping steam reforming to produce pure H_2 . Compared with the conventional steam reforming process, chemical looping process can co-produce pure H_2 and H_2 -rich syngas from COG without additional separation step, which is beneficial for the subsequent application.

More importantly, oxygen carriers are highly resistant to sulfide, which may reduce the cost of desulfurization pretreatment. Ksepko et al. [26] reported in detail the effect of H_2S on chemical looping combustion over Fe–Mn-based oxygen carriers, which showed that all oxygen carriers were very stable during the whole testing. No sulfide, sulfite or sulfate was detected on the oxygen carriers after long-term reaction. García-Labiano et al. [27] observed that the $\text{Fe}_2\text{O}_3/\gamma\text{-Al}_2\text{O}_3$ oxygen carriers can completely oxidize H_2S into SO_2 under all operating conditions in the fuel reactor, and SO_2 was detected in the gas outlet flow of the air reactor. This indicates that the formed SO_2 during the fuel conversion should release from the fuel reactor, and no sulfur species were adsorbed on the oxygen carrier. Iron sulfide is absent even at high H_2S concentrations. A recent publication by Wang et al. [28] also revealed that sulfur species was not observed through oxygen carriers during the chemical looping reforming of petroleum coke with high sulfur content.

One of the most important issues for chemical looping conversion of COG and water to pure H_2 and syngas is the design of suitable oxygen carriers. In general, metal oxides provide the basis for redox chemistry due to their unique surface and bulk properties. The perovskite-structured metal oxides (ABO_3 -typed oxides) with excellent structural stability and oxygen carrying capacity have stimulated the interest of many researchers [29,30]. As a representative of perovskite-type metal oxides, LaFeO_3 has been widely used in the process of chemical-looping reforming [23,25,31–37]. Dai and Mihai et al. [33,34] reported that LaFeO_3 is an excellent oxygen carrier for chemical looping methane partial oxidation, which exhibits excellent CO selectivity and cycling stability at high temperatures. In addition, LaFeO_3 can also be used for chemical looping steam methane reforming (CL-SMR) and chemical looping CO_2 methane reforming (CL-DR), although the activity for methane conversion is not satisfied [25,31,35]. With the deepening of research, it has been discovered that the oxygen storage capacity, lattice oxygen mobility and water splitting capacity of the perovskite-type oxygen carrier can be adjusted by partially replacing the A and/or B cations with other cations [38–42]. For 3DOM $\text{LaFe}_{1-x}\text{Ni}_x\text{O}_3$ system [36], although the CH_4 conversion is very high, the H_2/CO ratio of syngas is much higher than 2 and the H_2 purity in water splitting is not very high. It indicates that methane cracking occurs in the methane conversion step, which is a very undesirable phenomenon. In terms of Fe-substituted LaCoO_3 system [37], $\text{LaCo}_{0.6}\text{Fe}_{0.4}\text{O}_3$ showed best performance in chemical looping steam methane reforming and provided the highest extent of steam regeneration, hydrogen purity and enhanced selective oxidation of CH_4 to syngas, which was reflected in the 92% CO selectivity and 99.3% hydrogen purity with a produced amount of 2.22

mmol $\text{H}_2/\text{g}_{\text{cat}}$ at a relatively low temperature of $700\text{ }^{\circ}\text{C}$. Zhao et al. [39] synthesized a series of $\text{LaFe}_{1-x}\text{Co}_x\text{O}_3$ oxygen carriers and found that, with the doping amount of Co increasing to 30%, both the reactivity and resistance to carbon deposition of the oxygen carrier were significantly improved but the redox stability and CO selectivity were weakened. Similar phenomena were also observed over the $\text{LaMn}_x\text{Fe}_{1-x}\text{O}_3$ oxygen carriers, which showed high resistance to carbon deposition but low redox stability [40].

On the other hand, it is also reported that metal Ni can effectively activate methane via reducing the dissociation energy barrier of C–H bonds in heterogeneous catalytic reactions [43–45]. In this case, a variety of Ni promoted oxygen carriers have been widely studied. Ruan et al. [43] designed a Ni promoted Ce–Ti–O oxygen carrier for two-step solar thermal splitting of CO_2 or H_2O driven by methane reduction, and the results indicated that the metallic Ni and the Ni/oxide interface played an important role for both CH_4 activation and CO_2 or H_2O splitting. Shen et al. [36] designed a series of three-dimensionally ordered macroporous $\text{LaFe}_{1-x}\text{Ni}_x\text{O}_3$ perovskites and tested their performance in CL-SMR. They found that the conversion of methane was the highest (about 95%) when the content of Ni was 10%, but the carbon deposition was also very serious at the same time. The same phenomenon was also observed in $\text{La}_{0.7}\text{Sr}_{0.3}\text{Ni}_{0.05}\text{Fe}_{0.95}\text{O}_3$ [46]. Yan et al. and his co-workers [47] pointed out that $\text{LaNi}_{0.5}\text{Fe}_{0.5}\text{O}_3$ has good activity in chemical looping catalytic gasification of biomass process. The above researches indicate that nickel promoted oxygen carriers often show high activity for methane conversion, but the formation of carbon deposition is a main drawback.

In the present work, we prepared a robust and polyfunctional Ni-doped LaFeO_3 perovskite for chemical looping water splitting driven by coke oven gas reduction. The presence of Ni in the perovskite lattice as well as the exsolution of Ni particles on the surface not only enhanced the methane conversion during the COG reduction step but also increased the hydrogen yield during water splitting. The role of nickel species in accelerating methane activation and H_2O splitting was investigated in detail via designed experiments and DFT calculations. The formation of carbon deposition can be inhibited via fine tuning the content of Ni.

2. Experimental

2.1. Synthesis of $\text{LaNi}_x\text{Fe}_{1-x}\text{O}_{3-\lambda}$ oxygen carriers

$\text{LaNi}_x\text{Fe}_{1-x}\text{O}_{3-\lambda}$ ($x = 0, 0.01, 0.03, 0.05, 0.07, 0.1$) oxygen carriers were prepared by a sol-gel method. The required amounts of La (NO_3) $_3 \cdot 6\text{H}_2\text{O}$, Fe(NO_3) $_3 \cdot 9\text{H}_2\text{O}$ and Ni(NO_3) $_2 \cdot 6\text{H}_2\text{O}$ were added into deionized water with stirring to prepare a mixed solution. Then citric acid powder was added into the solution of the mixed nitrates with a citric acid /nitrates molar ratio of 1.05. Thereafter, the resulting solution was allowed to evaporate by stirring at $70\text{ }^{\circ}\text{C}$ until a viscous gel was obtained. The gel was dried at $120\text{ }^{\circ}\text{C}$ for 12 h and then calcined at $800\text{ }^{\circ}\text{C}$ for 3 h under air atmosphere. Before testing, the prepared $\text{LaNi}_x\text{Fe}_{1-x}\text{O}_{3-\lambda}$ is crushed and sieved to the desired sizes (20–40 meshes).

2.2. Material characterizations

Powder X-ray diffraction (XRD) patterns were performed to investigate the crystallographic phase of catalysts using a MiniFlex600 Rigaku X-ray Diffraction (XRD) meter with Cu K α radiation ($\lambda = 0.15406\text{ nm}$). The diffraction patterns were collected at ambient conditions between 2θ values of 10° and 90° with a step size of $2^{\circ} \cdot \text{min}^{-1}$.

Hydrogen-temperature programmed reduction (H_2 -TPR) was performed on a Quantachrome Instrument. After a standard cleaning pretreatment, 100 mg of catalyst in a U tube reactor was heated from room temperature to $900\text{ }^{\circ}\text{C}$ with a heating rate of $10\text{ }^{\circ}\text{C} \cdot \text{min}^{-1}$ in a flow of 10% H_2/Ar ($25\text{ mL} \cdot \text{min}^{-1}$).

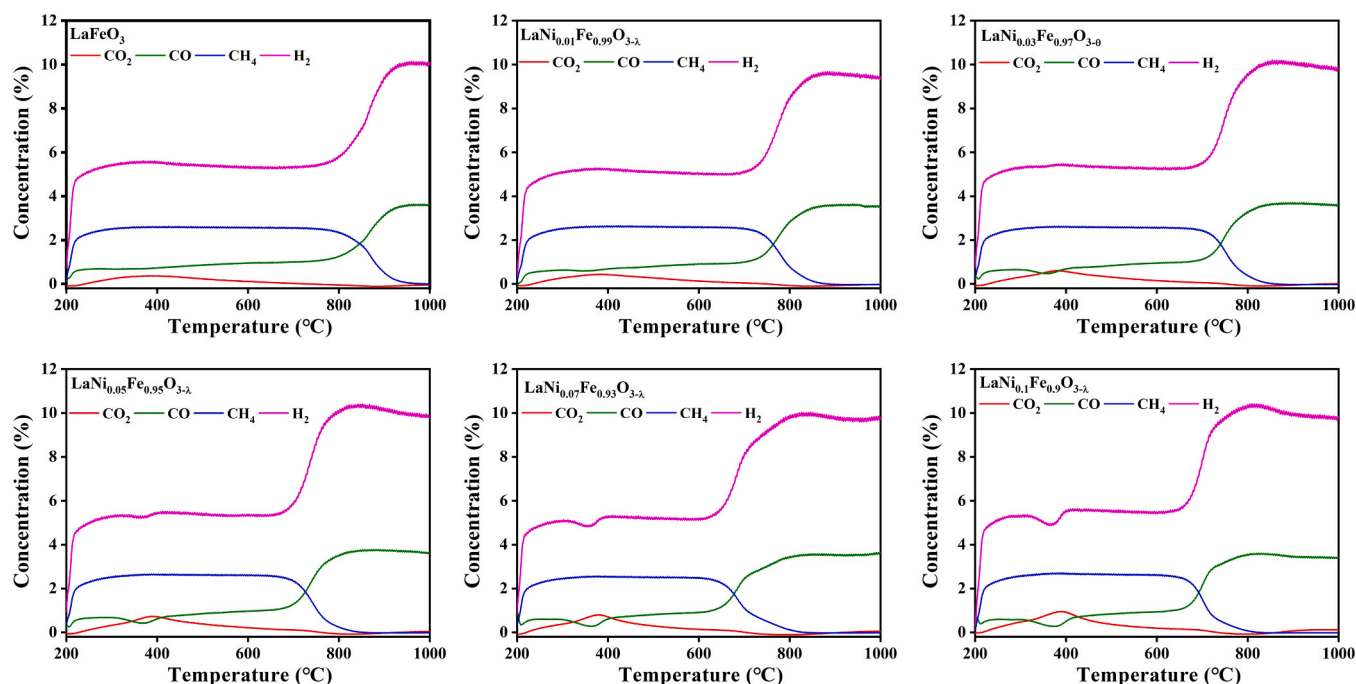


Fig. 1. COG-TPR profiles of the prepared $\text{LaNi}_x\text{Fe}_{1-x}\text{O}_{3-\lambda}$ oxygen carriers.

Scanning electron microscopy (SEM) technique (VERSA 3D, FEI) was used to examine the morphology of oxygen carriers. **Transmission electron microscopy (TEM)** was used a Tecnai G² TF30 S-Twin microscope operating at 300 kV. The specimens were crushed into a powder and immersed in a small volume of ethanol. After sonicating the mixture for 10 min, a droplet of the suspension was allowed to dry on a holey carbon/Formvar-coated copper TEM grid.

The X-ray photoelectron spectroscopy (XPS) experiments were carried out on a Thermo fisher Scientific K-Alpha⁺ system equipped with a monochromatic Al-Kα X-rays source. Spectra were registered after purging the samples at ambient temperature in vacuum (residual pressure < 10^{-7} Pa). An electron flood gun compensated sample charging during the measurement. The C 1s signal at 284.8 eV was used as an internal standard for calibration of the XPS-signals.

2.3. Activity tests

Temperature programmed reduction with coke oven gas (COG-TPR). The COG-TPR was performed in an atmospheric pressure fixed bed reactor (a quartz tube with 19 mm inside diameter). After the oxygen carriers (2 g) with a size range of 20–40 mesh were placed in the reactor, the reactor was heated to 200 °C at a heating rate of 10 °C·min⁻¹ under Ar atmosphere. Then, COG/Ar mixture gas (2.8% CH₄, 6.0% H₂, 0.3% CO₂, 0.9% CO and 90% high purity Ar) was introduced into the reactor instead of Ar at a flow rate of 150 mL·min⁻¹, which was accompanied the analysis of the outlet gas by the mass spectrometer.

Isothermal reaction with coke oven gas. The evaluation of oxygen carrier activity for COG conversion was carried out in the sample reactor with the COG-TPR experiment. After the oxygen carriers with a size of 20–40 mesh was placed into the reactor, it was firstly heated in pure Ar with a temperature ramp of 10 °C·min⁻¹ from RT to target temperatures (700, 800 and 900 °C), and then the COG (150 mL·min⁻¹) flowed through the reactor for reacting with the oxygen carriers. The outlet gases were monitored by the mass spectrometer.

Water splitting reaction. After the isothermal reaction with COG for 30 min, pure Ar (99.99%) was introduced to purge the reactor for 15 min instead of the COG. Then the steam was flowed through the reactor by using Ar (99.99%) as carrier gas. The outlet gases were monitored by

mass spectrometer.

Successive chemical looping cycle experiment. After the oxygen carrier (2.0 g) is reduced by COG (150 mL·min⁻¹) for 30 min, the heated steam is taken into the reactor by Ar carrier gas (150 mL·min⁻¹) to regenerate the oxygen carrier. These redox cycles were separated by a purge with pure Ar (150 mL·min⁻¹) for 10 min, to avoid mixing the gases arising during the two steps.

All the reactions of chemical looping were conducted under atmospheric pressure.

2.4. Computational details

All DFT calculations were performed using the DMol3 package from Materials Studio. The electron exchange correlation functions were calculated using Perdew–Burke–Ernzerh (PBE) functions within the generalized gradient approximation (GGA) [48]. All core electrons were represented by DFT semi-core pseudopotentials to reduce the computational cost. Brillouin zone was integrated using a grid of $1 \times 1 \times 1$ Monkhorst–Pack scheme after different k-point grid schedules was tested. As can be seen in Fig. 10(c), the HRTEM images reveal that small Ni particles are well dispersed on the surface of LaFeO₃ (121). The crystal structure of LaFeO₃ (121) with a space group Pn^{*}a was used and the Ni cluster structure with 7 atoms was anchored on the top of the LaFeO₃ (121) surfaces and the explicit surface structures are shown in Fig. S1.

The adsorption energies (E_{ads}) of H₂, CO, and CH₄ on the Ni7cluster@LaFeO₃ (121) surface were calculated using:

$$E_{\text{ads}} = E_{\text{H}_2/\text{CO}/\text{CH}_4 + \text{Ni7cluster@LaFeO}_3} - (E_{\text{H}_2/\text{CO}/\text{CH}_4} + E_{\text{Ni7cluster@LaFeO}_3}) \quad (1)$$

2.5. Calculation formulas

CH₄ conversion:

$$X_{\text{CH}_4}(\%) = \frac{\int_0^t C_{\text{CH}_4, \text{in}} dt \times F - \int_0^t C_{\text{CH}_4, \text{out}} dt \times F}{\int_0^t C_{\text{CH}_4, \text{in}} dt \times F} \quad (2)$$

CO yield:

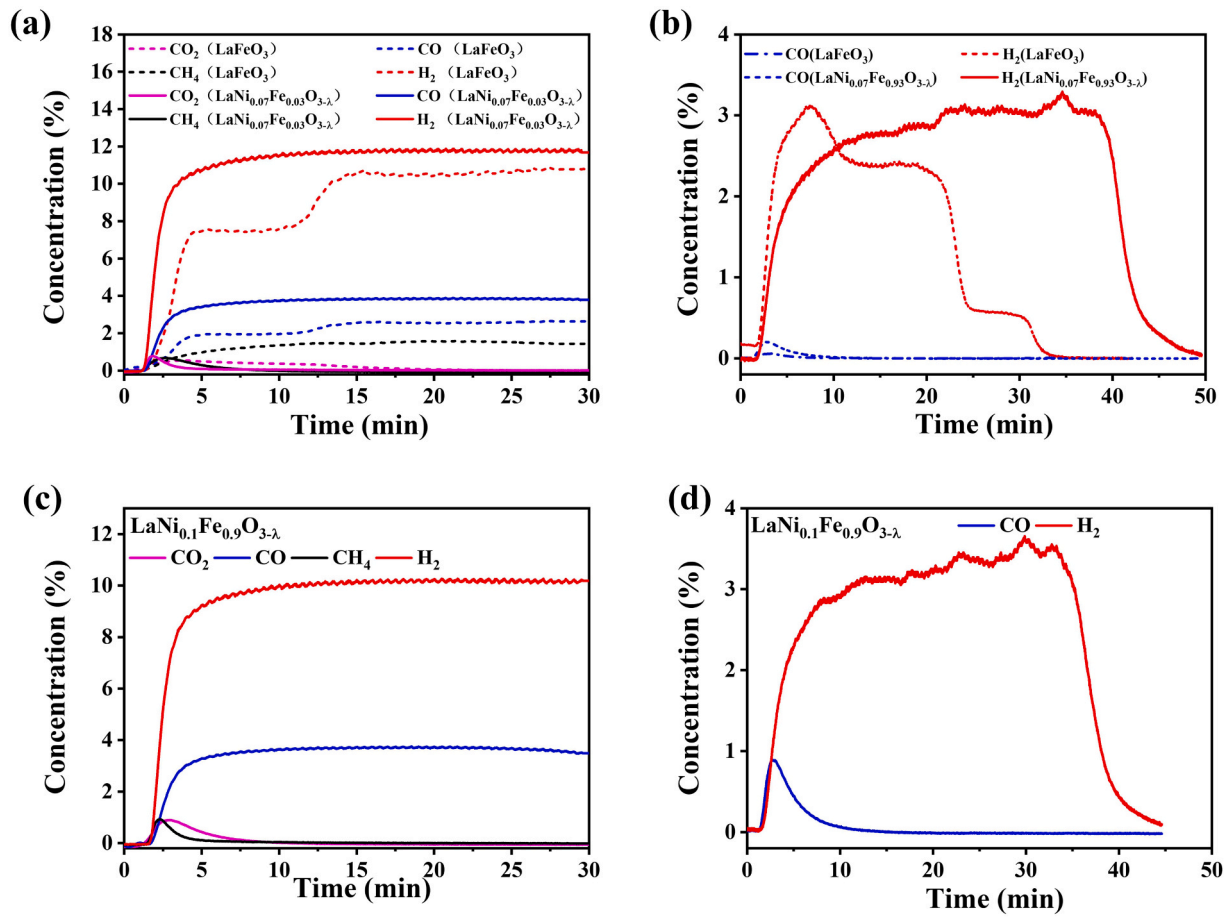


Fig. 2. (a) Evolution of the temporal gaseous product during the reactions of LaFeO₃ and LaNi_{0.07}Fe_{0.93}O_{3-λ} with COG and (b) the temporal gaseous product in water splitting step at 800 °C, (c) evolution of the temporal gaseous product during the reactions of LaNi_{0.1}Fe_{0.9}O_{3-λ} with COG and (d) the temporal gaseous product in water splitting step at 800 °C.

$$y_{CO} = \frac{\int_0^t C_{CO,out} dt \times F}{R \times m_{oxygen \text{ carrier}}} \quad (3)$$

H₂ yield:

$$y_{H_2} = \frac{\int_0^t C_{H_2,out} dt \times F}{R \times m_{oxygen \text{ carrier}}} \quad (4)$$

CO₂ yield:

$$y_{CO_2} = \frac{\int_0^t C_{CO_2,out} dt \times F}{R \times m_{oxygen \text{ carrier}}} \quad (5)$$

Ratio of H₂/CO:

$$P = \frac{\int_0^t C_{H_2,out} dt \times F}{\int_0^t C_{CO,out} dt \times F} \quad (6)$$

H₂ purity :

$$p_{H_2} = \frac{\int_0^t C_{H_2,out} dt \times F}{\int_0^t C_{CO,out} dt \times F + \int_0^t C_{H_2,out} dt \times F} \quad (\text{Only for water splitting step}) \quad (7)$$

Where C is real time concentration of gas, F is the gas flow rate, R is the volume of gas in an ideal state (22.4 L·mol⁻¹).

3. Results

3.1. Redox performance and stability

Fig. 1 shows the evolutions of H₂, CO, CH₄ and CO₂ during the temperature programmed reaction between COG and different oxygen carriers (COG-TPR). It can be seen that the concentration of H₂ is slightly lower than the theoretical value (6%) over each catalyst in the temperature range from 300 to 700 °C, indicating that small amount of H₂ is consumed by the catalysts. Meanwhile, a slight increase in the CO₂ concentration and a decrease in the CO and H₂ concentration are observed at temperatures lower than 400 °C, which should be related to the oxidation of CO and H₂ by the active surface oxygen species on the oxygen carriers. It is also noted that, with the increase of Ni content, the peaks for CO₂ formation and consumption of CO and H₂ are enhanced. These phenomena indicates that both H₂ and CO can be oxidized by the oxygen carriers at relative low temperatures (<400 °C), and the incorporation of Ni cations improves the concentration of reactive oxygen species.

When the reaction increases to higher than 750 °C, the concentration of methane sharply decreases, which is accompanied by the increase of H₂ and CO concentration, suggesting that methane could be partially oxidized to CO and H₂ at relatively high temperatures. The doping of Ni in LaFeO₃ reduces the initial temperature for methane oxidation on and produce more CO and H₂. It is worth noting that the initial temperature for methane oxidation decreases with increasing Ni contents, and it is only about 700 °C for methane conversion towards LaNi_{0.1}Fe_{0.9}O_{3-λ} sample. This phenomenon indicates that the nickel doping in LaFeO₃

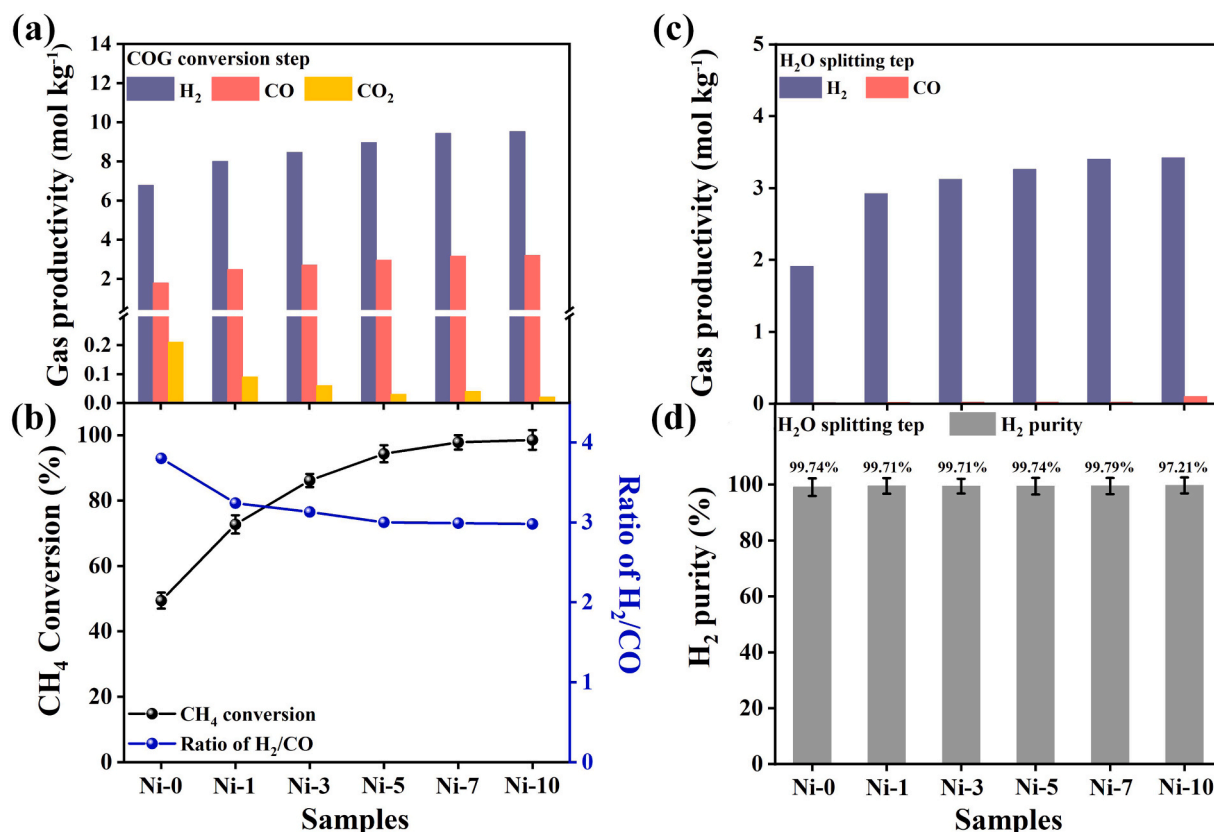


Fig. 3. (a) Yields of H₂, CO, CO₂ and (b) CH₄ conversion and H₂/CO ratio in COG conversion step over different LaNi_xFe_{1-x}O_{3-λ} oxygen carriers, (c) Yields of H₂, CO and (d) H₂ purity in H₂O splitting step.

phase promotes the conversion of methane at relatively lower temperatures. According to the COG-TPR results, 800 °C was chosen as the temperature for isothermal reaction.

The results in the isothermal reactions between COG and oxygen carriers as well as the hydrogen production via water splitting are presented in Fig. 2. Since all the catalysts shows similar trends for the evolutions of CH₄, H₂, CO and CO₂ during the reaction with COG, we only show the results from LaFeO₃, LaNi_{0.07}Fe_{0.93}O_{3-λ} and LaNi_{0.1}Fe_{0.9}O_{3-λ} in Fig. 2 for comparison. The results for other samples are shown in Fig. S2 in the supporting information. For the COG conversion step, there are three sources of hydrogen: 1) the original H₂ in feed gas, 2) generated H₂ via partial oxidation of methane and 3) generated H₂ from methane cracking. Similar, CO is also from three sources: 1) the original CO in feed gas, 2) generated CO via partial oxidation of methane and 3) generated CO from disproportionation of CO₂ or reversed water gas shift reaction. In terms of the water splitting step, H₂ is generated by

water splitting, while CO can be produced via oxidation of carbon deposition with water. The formation of carbon deposition in the COG conversion step must be avoided to produce high-purity H₂ in the water splitting step. In addition, we made a preliminary exploration on the sulfur resistance of LaNi_{0.07}Fe_{0.93}O_{3-λ} (seen in Fig. S3).

As can be seen from Fig. 2(a), methane conversion can be immediately observed when COG is introduced into the reactor, which result in a sharp increase in the concentration of H₂ and CO. The concentration of H₂ is almost doubled when comparing with initial value (6%) in the feed gas, while CO₂ quickly disappears with the reaction proceeding. It is also observed that the LaNi_{0.07}Fe_{0.93}O_{3-λ} catalyst shows much higher concentration of CO and H₂ as well as lower methane concentration than the LaFeO₃. By contrast, the amount of CO₂ over pure LaFeO₃ is higher than that over the LaNi_{0.07}Fe_{0.93}O_{3-λ} sample, indicating more unselective surface oxygen species on the pure LaFeO₃ sample that can oxidize methane to CO₂. In the water splitting step, the formation of H₂ with

Table 1

Summary of the integrated outlet gaseous species for LaNi_xFe_{1-x}O_{3-λ} oxygen carriers during chemical looping reforming of coke oven gas.

OCs	COG conversion step						H ₂ O splitting step		
	CH ₄ (mol·kg ⁻¹)	CO (mol·kg ⁻¹)	CO ₂ (mol·kg ⁻¹)	H ₂ (mol·kg ⁻¹)	H ₂ O (mol·kg ⁻¹)	O ^a (mol·kg ⁻¹)	H ₂ (mol·kg ⁻¹)	CO (mol·kg ⁻¹)	O ^b (mol·kg ⁻¹)
Ni-0	1.28	1.78	0.21	6.77	1.34	2.50	1.92	0.005	1.91
Ni-1	0.71	2.47	0.09	8.00	1.28	2.89	2.93	0.009	2.92
Ni-3	0.50	2.70	0.06	8.46	1.24	3.04	3.07	0.009	3.06
Ni-5	0.28	2.95	0.03	8.96	1.18	3.16	3.18	0.01	3.15
Ni-7	0.07	3.15	0.02	9.43	1.10	3.26	3.30	0.007	3.29
Ni-10	0.02	3.13	0.02	9.54	1.05	3.18	3.21	0.09	3.20
Blank ^c	2.53	0.47	0.28	5.63	—	—	—	—	—

^a The O²⁻ consumed during the reduction half cycle was derived from the reduction of LaNi_xFe_{1-x}O_{3-λ}.

^b The O²⁻ regenerated during the H₂O splitting half cycle.

^c Blank test under the same experimental conditions.

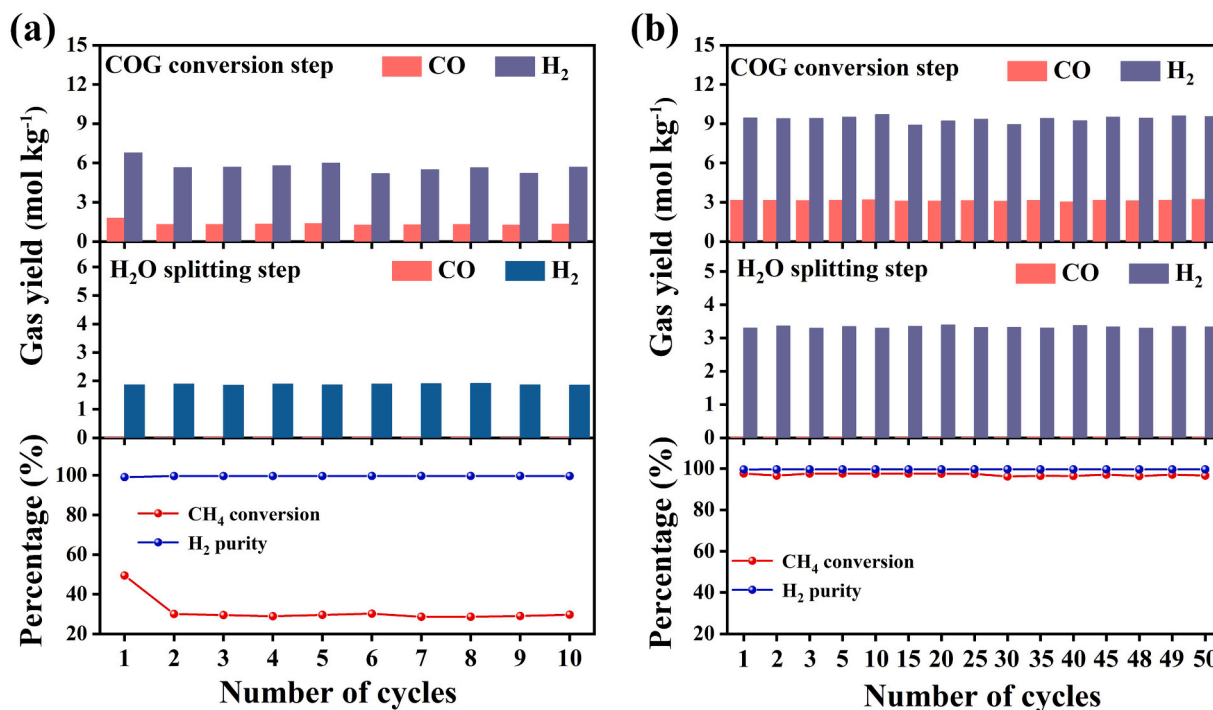


Fig. 4. Redox stability of LaFeO_3 (a) and $\text{LaNi}_{0.07}\text{Fe}_{0.93}\text{O}_{3-\lambda}$ (b) oxygen carriers for chemical looping steam COG reforming.

high concentration lasts for much longer time for $\text{LaNi}_{0.07}\text{Fe}_{0.93}\text{O}_{3-\lambda}$ than LaFeO_3 , and almost no CO is detected for both samples. However, when further increasing the Ni content to 10% ($\text{LaNi}_{0.1}\text{Fe}_{0.9}\text{O}_{3-\lambda}$), obvious CO is detected in the water splitting step (see Fig. 2(d)), indicating the formation of carbon deposition on the reduced oxygen carrier. This suggests that the enhanced methane conversion over the Ni doped LaFeO_3 without the formation of carbon deposition can be achieved by choosing suitable content of Ni (i.e., 7%), which is ideal for balancing the yield and purity of H_2 .

Fig. 3 show the quantitative analysis on the productivity of H_2 and CO, CH_4 conversion and the H_2/CO ratio in the COG conversion step as well as the yield and purity of H_2 in the water splitting steps over different catalysts. Table 1 summarizes the integrated outlet gaseous species over different $\text{LaNi}_x\text{Fe}_{1-x}\text{O}_{3-\lambda}$ oxygen carriers during chemical looping reforming of COG. In terms of the COG conversion step, H_2 and CO are the main products, which are strongly related to the methane conversion. As can be observed, for the single LaFeO_3 sample, the amount of consumed oxygen (O^a in Table 1) in the COG conversion step is a little higher than the supplementary oxygen (O^b in Table 1) in the water splitting step (2.50 vs $1.91 \text{ mol}\cdot\text{kg}^{-1}$). Quantitative analysis indicates that only 76.4% of consumed oxygen in the LaFeO_3 can be recovered via water oxidation. However, it is interesting that, when Ni is incorporated into the LaFeO_3 sample, the amount of consumed oxygen increases, and all the oxygen consumed in the COG conversion step can be recovered in the water splitting step. This indicates that the presence of Ni in LaFeO_3 can enhance both the activity of oxygen carrier for COG conversion and the regeneration of reduced oxygen carrier via water splitting. Since the carbon deposition from methane cracking inevitably results in the formation of CO via water oxidation, the trace CO formed in the water splitting step indicates that very limited methane cracking occurs in the methane oxidation step over the $\text{LaNi}_{0.07}\text{Fe}_{0.93}\text{O}_{3-\lambda}$ sample.

As can be seen in Fig. 3(a) and (b), the addition of Ni in LaFeO_3 catalyst significantly improves the methane conversion and increase the yields of both CO and H_2 , especially for the samples with relatively high Ni loadings (e.g., $\text{LaNi}_{0.07}\text{Fe}_{0.93}\text{O}_{3-\lambda}$ and $\text{LaNi}_{0.1}\text{Fe}_{0.9}\text{O}_{3-\lambda}$). Almost 100% of methane can be converted for the $\text{LaNi}_{0.07}\text{Fe}_{0.93}\text{O}_{3-\lambda}$ and $\text{LaNi}_{0.1}\text{Fe}_{0.9}\text{O}_{3-\lambda}$ samples. In addition, the H_2 yield in the water splitting step

(Fig. 3(c) and (d)) also increases with the increase of Ni content, and all the samples for Ni content lower than 10% show high purity of produced H_2 ($> 99\%$). The $\text{LaNi}_{0.07}\text{Fe}_{0.93}\text{O}_{3-\lambda}$ sample show a H_2 yield at $3.30 \text{ mol}\cdot\text{kg}^{-1}$, which is raised by 70% compared with the pure LaFeO_3 . It is also noted that further increasing the Ni content from 7% to 10% fails to obviously enhance the methane conversion in the COG oxidation step and the formation of H_2 in the water splitting step. In addition, taking the relatively low purity of H_2 for the $\text{LaNi}_{0.1}\text{Fe}_{0.9}\text{O}_{3-\lambda}$ into account, the optimized molar content of Ni in LaFeO_3 is 7%.

Based on the results of isothermal reaction (Figs. 2 and 3), LaFeO_3 and $\text{LaNi}_{0.07}\text{Fe}_{0.93}\text{O}_{3-\lambda}$ were selected for continuous COG conversion/ H_2O splitting redox cycling test, and the results are shown in Fig. 4. As observed in Fig. 4(a), the CH_4 conversion is about 50% over the fresh LaFeO_3 , but it remarkably decreases to 30% after the first cycle. This indicates that the reduced LaFeO_3 cannot be regenerated back to its initial state via H_2O splitting, which is very similar to our previous observation[49]. In this case, only ten redox cycles were performed on this sample. In the term of $\text{LaNi}_{0.07}\text{Fe}_{0.93}\text{O}_{3-\lambda}$ (Fig. 4(b)), the CH_4 conversion is almost 100% and keeps stable during 50 redox cycles, which results in very high yields of H_2 (ca $0.943 \text{ mol}\cdot\text{kg}^{-1}$) and CO (ca $0.315 \text{ mol}\cdot\text{kg}^{-1}$) in the COG conversion step and H_2 (ca $0.33 \text{ mol}\cdot\text{kg}^{-1}$) in the water splitting step. This indicates that the addition of Ni not only strongly enhance the activity of LaFeO_3 for methane conversion but also promote the redox stability. In addition, purity of H_2 during the water splitting step remains higher than 99.7% during the 50 redox cycles.

The effect of reaction temperatures (700, 800 and 900 °C) on the reactivity of LaFeO_3 and $\text{LaNi}_{0.07}\text{Fe}_{0.93}\text{O}_{3-\lambda}$ for methane conversion in COG oxidation and in H_2 generation from water splitting are also investigated, and the results are presented in Fig. 5 and Fig. S4. As can be seen in Fig. 5(a), the pure LaFeO_3 is inactive for methane conversion at 700 °C, and the concentration of syngas (CO and H_2) is lower than that in the original COG, indicating some of the CO and H_2 is consumed by the LaFeO_3 . On the other hand, a methane conversion at 45% is observed for the $\text{LaNi}_{0.07}\text{Fe}_{0.93}\text{O}_{3-\lambda}$ sample at 700 °C, and more CO and H_2 are also detected. This indicates that the presence of Ni significantly improves the activity of LaFeO_3 for methane conversion to syngas at relatively low temperatures. When the reaction temperature increases to 800 °C,

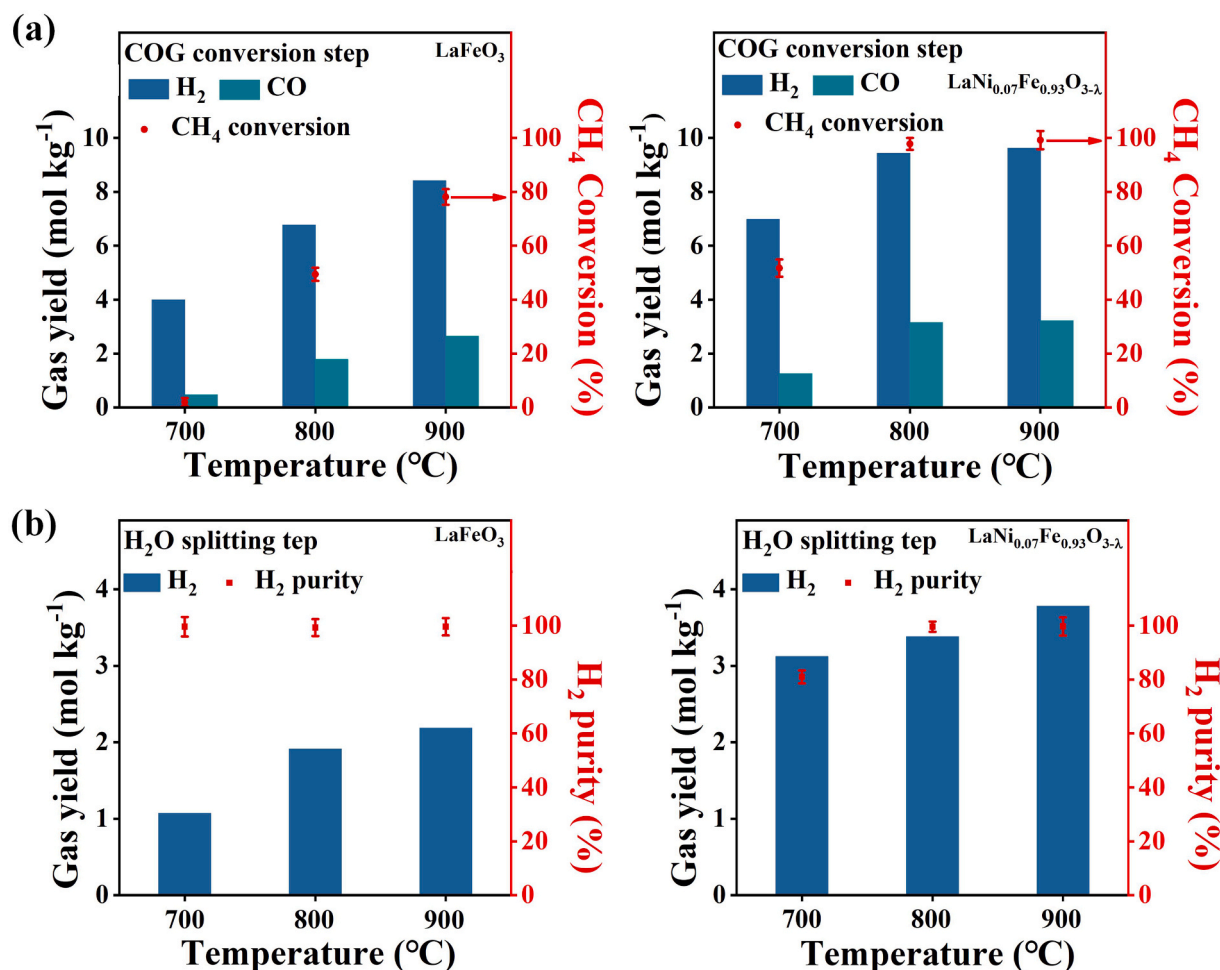


Fig. 5. Effect of reaction temperature on the LaFeO₃ and LaNi_{0.07}Fe_{0.93}O_{3-λ} oxygen carriers for chemical looping reforming of COG: (a) Yields of H₂, CO and CH₄ conversion in COG conversion and (b) Yields of H₂ and H₂ purity in H₂O splitting step.

almost 100% of methane can be converted to CO and H₂, which results in high yield of syngas. Further increasing the reaction temperature to 900 °C cannot increase the syngas yield. For the LaFeO₃ sample, it only shows relative high activity for methane conversion at 900 °C, but the syngas yield is still lower than that obtained from the LaNi_{0.07}Fe_{0.93}O_{3-λ} at 800 °C.

3.2. Physicochemical features of the catalysts

In order to clarify the potential reasons for the high activity of LaNi_{0.07}Fe_{0.93}O_{3-λ} oxygen carriers, various physicochemical characterizations are performed. Fig. 6(a) shows the XRD patterns of the as-prepared LaNi_xFe_{1-x}O_{3-λ} oxygen carriers. The diffraction peaks of all samples match well with LaFeO₃ perovskite phase (JCPDS card [37–1493]), and no impurity is observed. This indicates that all the initial synthesized LaNi_xFe_{1-x}O_{3-λ} samples show a well-formed perovskite structure. In order to explore the structure change of perovskite after Ni doping, Rietveld refinement calculation was performed on the XRD patterns of the LaFeO₃ and LaNi_{0.07}Fe_{0.93}O_{3-λ} samples, and the results were shown in Fig. 6(b) and (c) as well as Table S1 in the Supporting information. As can be seen in Table S1, R_{wp} of both samples is below 10%, and the χ^2 is also around 1.0, which indicates the refined results show high reliability because of the good match between the theoretical model and the actual test data. It can be concluded that the doping of Ni in LaFeO₃ lattice is achieved by replacing parts of Fe³⁺ at B-site. In this case, the cell parameter (a, b, c) of LaNi_{0.07}Fe_{0.93}O_{3-λ} is slightly larger than that of the pure LaFeO₃ due to the larger Ni²⁺ radius

(0.069 nm) than Fe³⁺ (0.0645 nm).

Fig. 7 shows the H₂-TPR profiles and hydrogen consumption of the LaNi_xFe_{1-x}O_{3-λ} oxygen carriers. The LaFeO₃ mainly exhibits two reduction peaks, with the first peak in the range from 490 to 550 °C and the second peak in the range of 590–800 °C. The low-temperature peak can be attributed to the consumption of surface adsorbed oxygen on LaFeO₃ and the reduction of Fe³⁺ to Fe²⁺, and the high-temperature peak with a shoulder at 640 °C is related to the consumption of bulk lattice oxygen and the reduction of Fe²⁺ to Fe [49,50]. When Ni is doped, the reduction peaks remarkably shift to low temperatures, and higher Ni content results in lower reduction temperature and higher peak intensity. It is worthy to stress that high-temperature peaks almost disappear with the increasing in Ni content. For the LaNi_{0.07}Fe_{0.93}O_{3-λ} and LaNi_{0.1}Fe_{0.9}O_{3-λ} samples, only one strongly enhanced main reduction peak can be observed at temperatures lower than 400 °C, and the quantitative analysis on the hydrogen consumption shows that most of the lattice oxygen has been consumed during this process (see Fig. 7(b)). In general, bulk lattice oxygen in perovskite oxide is relatively inactive, which can only be reduced at relatively high temperatures [51]. It also can be seen from Fig. 7(b) that the total hydrogen consumption of LaNi_xFe_{1-x}O_{3-λ} oxygen carriers increases with the increase of Ni doping. The above phenomenon reveals that the more lattice oxygen in LaFeO₃ can be reduced at low temperatures due to the Ni loading, indicating significantly improved lattice oxygen mobility at low temperatures.

It can be found from Fig. 4 that syngas yield and CH₄ conversion over LaFeO₃ decreased significantly during the second cycle and then the gases contents maintain at a relatively stable level, while yield of syngas

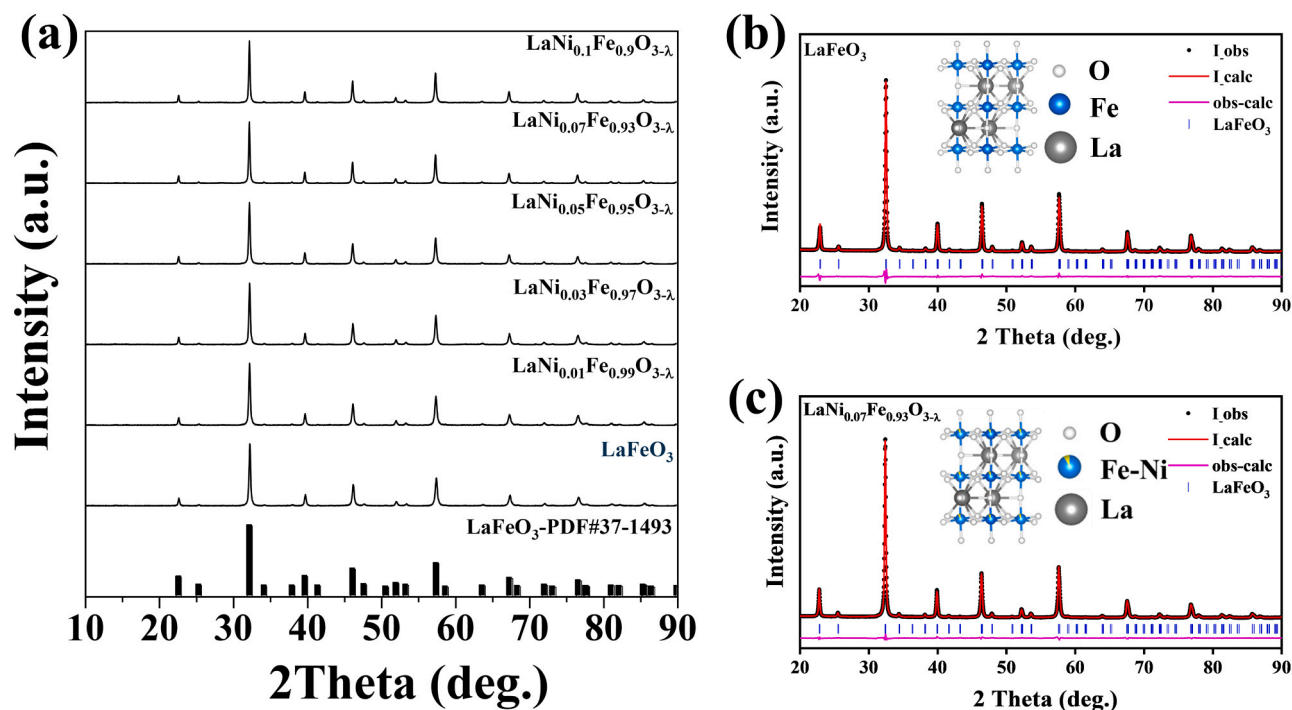


Fig. 6. X-ray powder diffraction patterns of the prepared $\text{LaNi}_x\text{Fe}_{1-x}\text{O}_{3-\lambda}$ oxygen carriers (a) and the Rietveld refinement results of XRD patterns: (b) LaFeO_3 , (c) $\text{LaNi}_{0.07}\text{Fe}_{0.93}\text{O}_{3-\lambda}$.

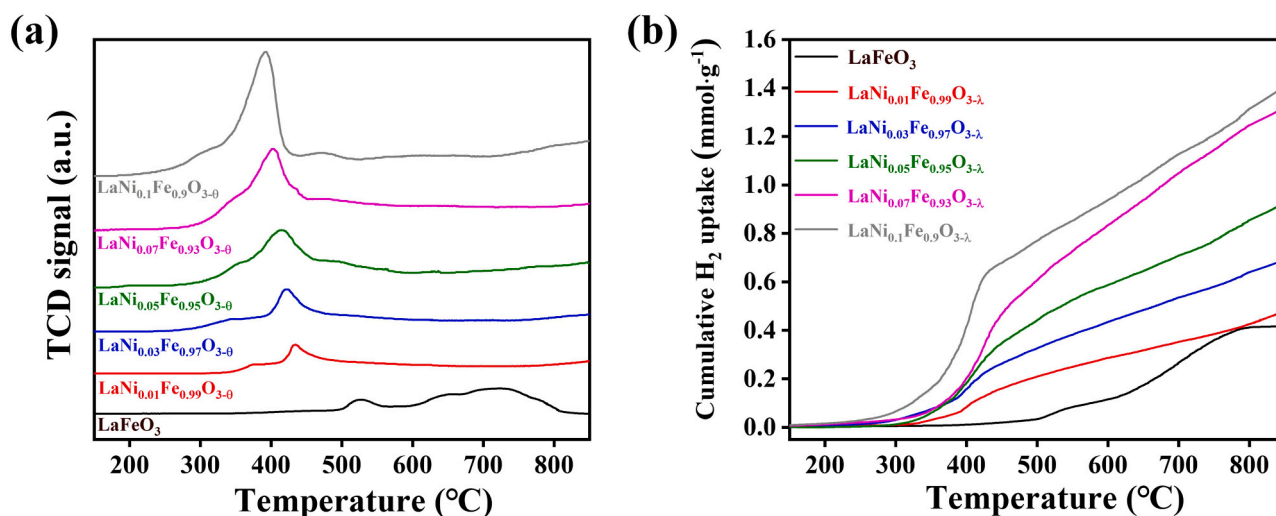


Fig. 7. H_2 -TPR profiles (a) and cumulative H_2 uptake (b) of the prepared $\text{LaNi}_x\text{Fe}_{1-x}\text{O}_{3-\lambda}$ oxygen carriers.

over $\text{LaNi}_{0.07}\text{Fe}_{0.93}\text{O}_{3-\lambda}$ keep stable during the cycling. Fig. 8(a1) and (b1) illustrate respectively the XRD patterns of the LaFeO_3 and $\text{LaNi}_{0.07}\text{Fe}_{0.93}\text{O}_{3-\lambda}$ oxygen carriers before and after long-term redox cycle. The crystal structures of as synthesized LaFeO_3 and $\text{LaNi}_{0.07}\text{Fe}_{0.93}\text{O}_{3-\lambda}$ samples match well with the orthorhombic unit cell of LaFeO_3 without any impurity phases. However, the typical characteristic peaks corresponding to La_2O_3 at 15.6° , 27.3° , 27.9° and 58.8° are detected in the cycled LaFeO_3 , indicating that the perovskite structure cannot be recovered by the reoxidation of H_2O . On the other hand, the cycled $\text{LaNi}_{0.07}\text{Fe}_{0.93}\text{O}_{3-\lambda}$ show the same XRD pattern with the fresh sample, which reveals that the crystallite state of $\text{LaNi}_{0.07}\text{Fe}_{0.93}\text{O}_{3-\lambda}$ has been totally restored.

Additionally, H_2 -TPR experiment was also performed as synthesized and the cycled LaFeO_3 and $\text{LaNi}_{0.07}\text{Fe}_{0.93}\text{O}_{3-\lambda}$ samples to investigate the redox stability, as shown in Fig. 8(a2) and (b2). The cycled

$\text{LaNi}_{0.07}\text{Fe}_{0.93}\text{O}_{3-\lambda}$ sample shows a H_2 -TPR profile similar to that of the fresh sample. In the case of the LaFeO_3 sample, the high-temperature reduction peak disappears after the redox cycling. In general, the higher temperature reduction peak is caused by the consumption of bulk lattice oxygen [51]. The disappearance of the high-temperature reduction peak should be due to the partial destruction of the LaFeO_3 structure as well as the sintering of the oxygen carrier, as observed in the XRD experiments.

X-ray photoelectron spectroscopy (XPS) was employed to shed light on the evolution of the surface O, Fe and Ni species of the LaFeO_3 and $\text{LaNi}_{0.07}\text{Fe}_{0.93}\text{O}_{3-\lambda}$ oxygen carriers at various stages. The O 1s spectra of the as synthesized, reduced and regenerated LaFeO_3 and $\text{LaNi}_{0.07}\text{Fe}_{0.93}\text{O}_{3-\lambda}$ oxygen carriers are displayed in Fig. 9(a1) and (b1), and detailed XPS spectra of the Fe 2p core level for the different LaFeO_3 and $\text{LaNi}_{0.07}\text{Fe}_{0.93}\text{O}_{3-\lambda}$ oxygen carriers are shown in Fig. 9(a2) and (b2). As

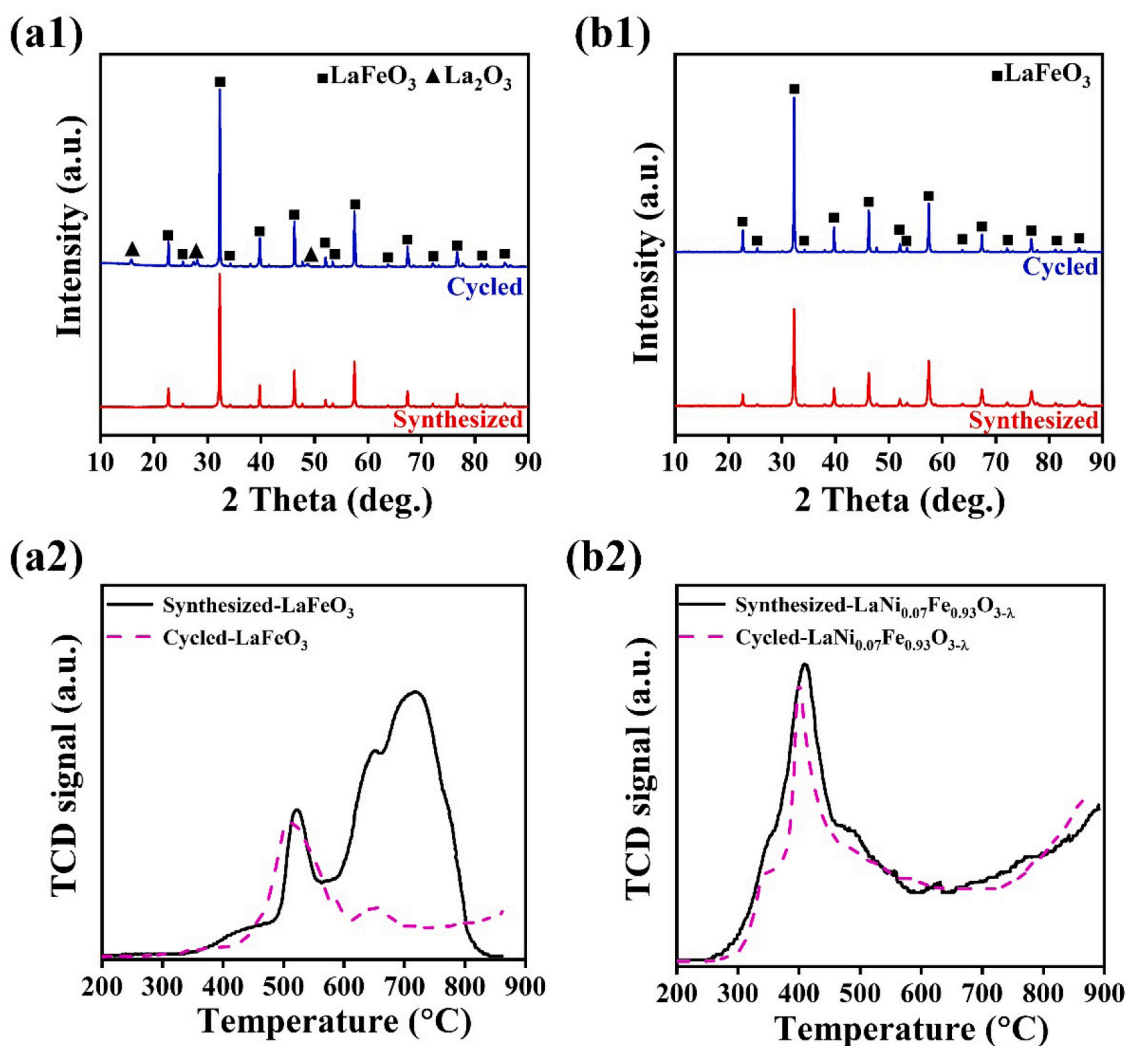


Fig. 8. X-ray powder diffraction patterns of the LaFeO₃ (a1) and LaNi_{0.07}Fe_{0.93}O_{3-λ} (b1) oxygen carriers at various stages (after synthesis and after redox cycle). And H₂-TPR profiles of the LaFeO₃ (a2) and LaNi_{0.07}Fe_{0.93}O_{3-λ} (b2) oxygen carriers at various stages (after synthesis and after redox cycle).

can be seen in Fig. 9(a1) and (b1), the deconvolution of the O 1 s band shows three distinct components. The predominant component at about 529.5 eV (labelled as OI) agrees well with the signature of lattice oxygen, while the two minor components centered at 531.8 eV (labelled as OII) and 533.2 eV (labelled as OIII) may be related to low coordination surface absorbed oxygen species (e.g., hydroxyl and carbonate species) [52]. In general, the concentration of the surface absorbed oxygen species can be enhanced by increasing the specific surface area or creating more oxygen vacancies of catalysts. In the present work, no obvious increase in the specific surface area (LaFeO₃: 6.6 m²/g vs LaNi_{0.07}Fe_{0.93}O_{3-λ}: 7.3 m²/g) is observed after the Ni doping. In this case, the OII and OIII signals should be related to the presence of oxygen vacancies. As the previous works reported, the concentration of surface oxygen vacancies can be estimated from the ratio (O_{ads}/O_{latt}) of oxygen species (O_2^{2-} or O^-) related to the surface oxygen vacancies to the lattice oxygen species determined by XPS [31]. The ratios OII/OI for fresh LaNi_{0.07}Fe_{0.93}O_{3-λ} shown in Table 2 are higher than those for LaFeO₃, which indicates that Ni doping promotes the formation of oxygen vacancy.

The as synthesized samples showed three strong peaks at 712.5 eV, 713.5 eV and 724 eV along with a broad satellite peak at 716.7 eV, which could be assigned to the Fe³⁺ in LaFeO₃. After the COG reduction step, a peak at 709.9 eV associated with divalent metal Fe²⁺ is clearly identified [53]. Apparently, for LaNi_{0.07}Fe_{0.93}O_{3-λ} samples after

regeneration step, the peak of Fe²⁺ disappears, which indicates that Fe²⁺ is converted to Fe³⁺ by H₂O. However, for LaFeO₃ samples, there are still a lot of divalent iron ions Fe²⁺ after regeneration. This indicates that Ni species contribute to the reconstruction of perovskite structure during the water splitting step. Furthermore, the Ni 2p_{3/2} spectra of LaNi_{0.07}Fe_{0.93}O_{3-λ} samples are shown in Fig. S5. It suggests that Only Ni²⁺ exists in the fresh sample, while metallic Ni and Ni²⁺ co-exist in both the reduced and the regenerated samples.

SEM and TEM measurements were also performed on the LaNi_{0.07}Fe_{0.93}O_{3-λ} sample before and after redox cycle at 800 °C, with the results reported in Fig. 10. For the initial synthetic sample (Fig. 10(a)), the Ni element region almost overlaps with the La and Fe element regions, which indicates that the Ni cations in LaNi_{0.07}Fe_{0.93}O_{3-λ} lattice are uniformly dispersed. After recycling (see Fig. 10(b)), the all the elements show similar dispersion with the fresh ones, and no agglomeration of Ni or other elements is detected. For the SEM images, very slight increase in the particles of oxygen carrier is observed for the recycled sample. All the above phenomena indicate that the microstructure of LaNi_{0.07}Fe_{0.93}O_{3-λ} sample keep stable during the 50-cycle redox test, which should contribute to the high stability in the chemical looping process for the successive generation of syngas and H₂ from COG and H₂O. In addition, after the reaction with COG for about 3 min, the presence of exsolved Ni particles on the surface of LaFeO₃-based perovskite can be evidenced by the high-resolution TEM measurement, as shown in Fig. 10

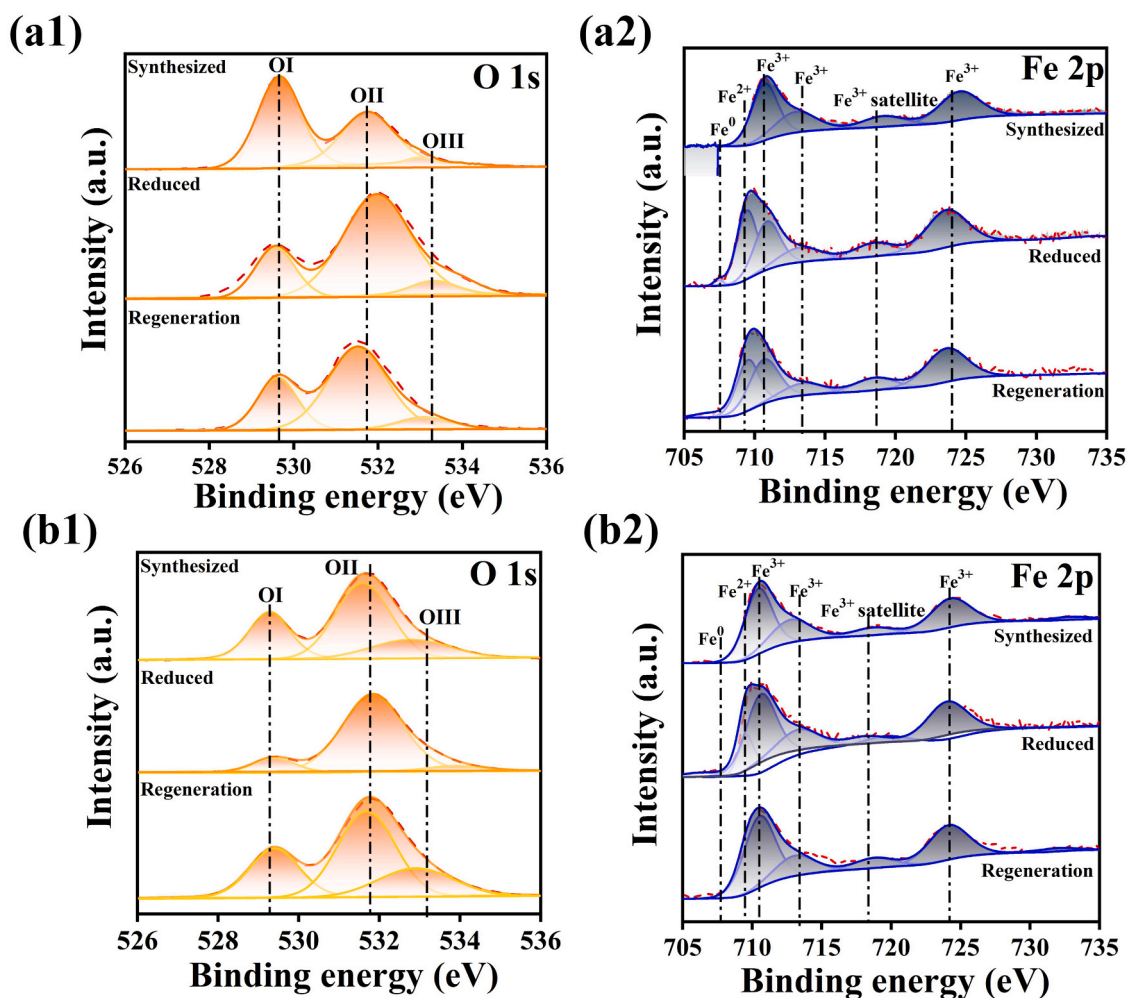


Fig. 9. XPS spectra for O 1s (1) and Fe 2p (2) over LaFeO₃ (a) and LaNi_{0.07}Fe_{0.93}O_{3-λ} (b) at various stages (as synthesized, COG reduced and H₂O regenerated).

Table 2

XPS-Derived Characteristics of LaFeO₃ and LaNi_{0.07}Fe_{0.93}O_{3-λ} oxygen carriers at various stages.

Oxygen carriers	Stages	Oxygen species percent (%)			(OI+OII)/OIII
		OI	OII	OIII	
LaFeO ₃	Synthesized	62	32	6	0.61
	COG reduced	25	65	10	3
	H ₂ O regenerated	28	69	3	2.57
LaNi _{0.07} Fe _{0.93} O _{3-λ}	Synthesized	31	54	15	2.23
	COG reduced	12	84	4	7.3
	H ₂ O regenerated	13	56	11	2.03

(c). As can be seen, the HRTEM images reveal that small Ni particles are well dispersed on the surface of LaFeO₃. On the other hand, the results in Fig. 2 show that the conversion of methane is strongly enhanced after the reaction proceeding for 3 min. This may be related with the presence of isolated Ni particles, because Ni is one of the most active catalysts for enhancing methane conversion in many reactions.

4. Discussion on possible reaction mechanism

The above observations reveal that the presence of Ni species is vital for catalyzing CH₄ activation at lower temperature. Huang et al. [54] found that the NiO-modified Fe₂O₃ can significantly increase the reducibility of Fe₂O₃. Ruan et al. [43] reported that the metallic Ni and

the Ni/oxide interface manifest catalytic activity for CH₄ activation. In general, the cation doping into the bulk of LaFeO₃ can weaken the Fe–O bond strength, reduce the barrier of oxygen migration [55]. Comparably, the doping of Ni ions into LaFeO₃ may weaken the Fe–O bond strength and improve the mobility of lattice oxygen, catalyzing partial oxidation of methane in COG with an enhanced methane conversion and syngas yield.

From Table 1 and Fig. 1, it can be concluded that LaNi_{0.07}Fe_{0.93}O_{3-λ} sample can preferentially convert methane with the presence of CO and H₂ at high temperatures. In order to further explain the experimental phenomena, we performed the DFT calculations on the adsorption energy of H₂, CO and CH₄ on practically reduced LaNi_{0.07}Fe_{0.93}O_{3-λ} with the presence of Ni clusters. In general, LaFeO₃ shows the most stable crystal plane (121), which is supported by results of XRD and TEM measurements. According to the above information, the modelling in DFT calculation is performed as follow: the crystal structure of LaFeO₃(121) with a space group Pn^{*}a was used and the Ni cluster structure with 7 atoms was anchored on the top of the LaFeO₃ (121) surfaces. As far as Fig. 11 is concerned, the adsorption energy of methane ($E_{\text{abs, CH}_4} = -6.72\text{eV}$) on the surface of Ni cluster@LaFeO₃(121) is significantly greater than that of CO and H₂ ($E_{\text{abs, H}_2} = -4.25\text{eV}$, $E_{\text{abs, CO}} = -0.96\text{eV}$). This indicates that the CH₄ adsorption process is a highly stable exothermic reaction, although the three adsorption processes are still exothermic. It is also found that the adsorption and dissociation of methane on the interface between Ni clusters and LaFeO₃ are simultaneous, which is similar with the conclusions by Lee et al. [56] and Chorkendorff et al. [57]. Therefore, the

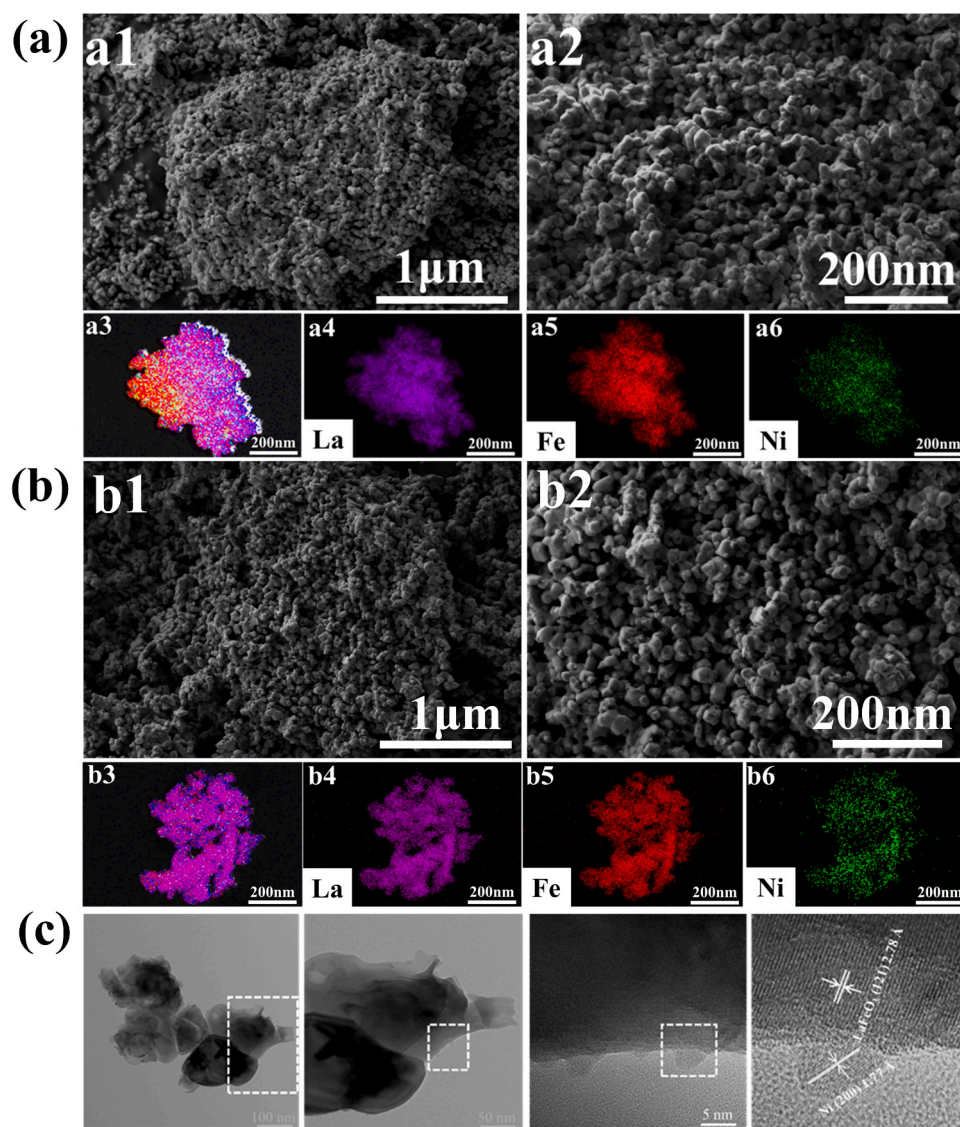


Fig. 10. SEM-EDS (a1, a2, b1, b2) and TEM-EDS (a3–6 and b 3–6) images of the (a) synthesized and (b) cycled $\text{LaNi}_{0.07}\text{Fe}_{0.93}\text{O}_{3-\lambda}$ oxygen carrier. The HRTEM images (c) for $\text{LaNi}_{0.07}\text{Fe}_{0.93}\text{O}_{3-\lambda}$ samples treated by COG reduced 3 min.

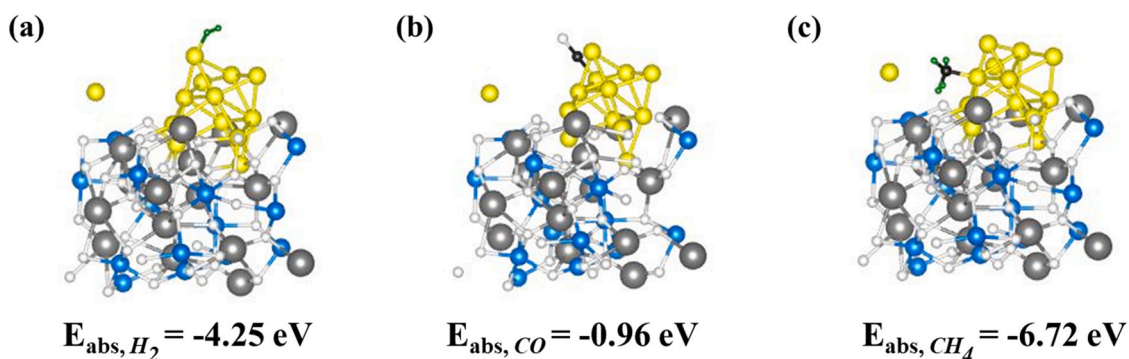


Fig. 11. Comparison of adsorption energies for H_2 (a), CO (b) and CH_4 (c) on the $\text{Ni}_7\text{cluster@LaFeO}_3$ (121) surface. O atoms are white, La atoms are gray, Fe atoms are blue, Ni atoms are yellow, C atoms are black and H atoms are green.

calculation results show that practically reduced $\text{LaNi}_{0.07}\text{Fe}_{0.93}\text{O}_{3-\lambda}$ with Ni clusters on the surface adsorbs CH_4 more easily than H_2 and CO .

In case of H_2O splitting step, H_2O molecules are converted to hydrogen while O is taken away by the low-valence cations in the reduce

oxygen carriers to restore the perovskite structure [31,58]. In this process, both the activation of H_2O and the reduction degree of oxygen carrier can affect the H_2O splitting. As observed above, the presence of Ni significantly improves the conversion of methane in COG, which will

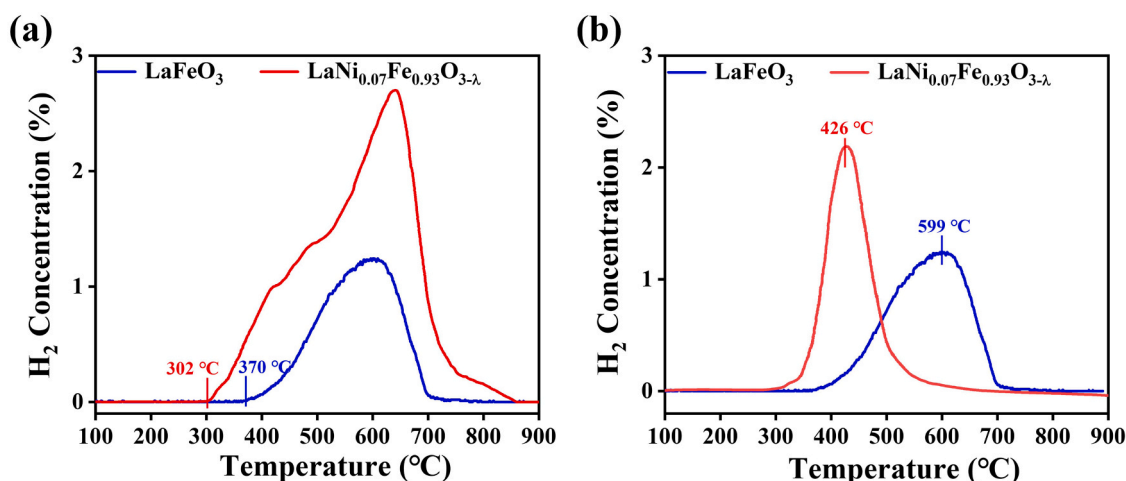


Fig. 12. H₂O-TPO over the LaFeO₃ and LaNi_{0.07}Fe_{0.93}O_{3-λ} oxygen carriers (a) pre-treated by 30 min of COG reduction and (b) with the same reduction degree.

increase the reduction degree of LaFeO₃ with the same reduction time. To further identify the role of Ni during H₂O splitting, the LaFeO₃ and LaNi_{0.07}Fe_{0.93}O_{3-λ} sample with fixed reduction degree were also prepared by changing the reaction time. H₂O oxidation performance of the reduced LaFeO₃ and LaNi_{0.07}Fe_{0.93}O_{3-λ} with fixed reduction time or reduction degree were evaluated with a H₂O-TPO experiment, as shown in Fig. 12. For the samples with fixed reduction time, the oxygen carriers were pre-reduced under the COG atmosphere at 800 °C for 30 min. As shown in Fig. 12(a), both LaFeO₃ and LaNi_{0.07}Fe_{0.93}O_{3-λ} oxygen carriers show activity for the water splitting with the formation of H₂ at very low temperatures, and the formation of H₂ is enhanced by increasing the reaction temperature. It should be highlighted that the formation of H₂ starts at 302 °C for the reduced LaNi_{0.07}Fe_{0.93}O_{3-λ} oxygen carrier, which is about 70 °C lower than that of reduced pure LaFeO₃. In addition, much higher intensity of H₂ is observed on the LaNi_{0.07}Fe_{0.93}O_{3-λ} sample due to the relative higher reduction degree. When fixing the reduction degree (Fig. 12(b)), the peak of H₂ evolution obviously shifts from 599 °C to 426 °C due to the presence of Ni, indicating that the Ni species must enhance the decomposition of H₂O molecules at relatively temperatures.

It has been reported that H₂O went through decomposition on the oxygen vacancies and reacted with adjacent O²⁻ species at the same time to produce OH⁻ first [59,60], and then O²⁻ ions are formed to restore the metal cations via the reforming of couple OH⁻ ions, accompanied by the generation of H₂. In addition, Carrasco et al. [61] found that the nickel species could lead to lower activation barrier for H₂O dissociation in the water-gas shift reaction. As water vapor is introduced on the surface of the reduced perovskite, the H₂O molecule is dissociated by oxygen vacancies on the surface and Ni species can accelerate this process, which acts as an electron donor and an active site of catalyst for H-O bond breaking, forming an OH⁻ and an H⁺. The OH groups formed on the Ni doped LaFeO₃ system upon dissociation, remain moderately bound to the Ni atoms and can therefore participate in generating H₂ meanwhile forming an O²⁻. Then the O²⁻ ions would be taken by the oxygen vacancies in the oxygen carrier, along with the oxidation of metals and/or metal cations with lower valence in the B-site of perovskite. In the present work, the nickel species also show positive role for enhancing H₂O dissociation. In addition, the LaNi_{0.07}Fe_{0.93}O_{3-λ} sample represents higher reduction degree than the pure LaFeO₃ with fixed reaction time, which would result in higher concentration of oxygen vacancy. In this case, the relatively high activity of LaNi_{0.07}Fe_{0.93}O_{3-λ} sample for H₂O splitting may be attributed to the synergistic effect of the higher oxygen vacancy concentration and the presence of nickel species. Ni atoms with catalytic function can promote and accelerate the surface reaction between oxygen vacancy and H₂O. The above experiment and

calcination results indicates that the nickel species in LaNi_{0.07}Fe_{0.93}O_{3-λ} oxygen carriers can promote both the activation of methane in coke oven gas to syngas and the splitting of H₂O to H₂.

5. Conclusions

We have demonstrated that LaFeO₃ oxygen carrier with suitable amount of nickel doping are effective for the chemical looping water splitting to produce syngas and H₂ by using COG as reducing agent. The LaNi_{0.07}Fe_{0.93}O_{3-λ} oxygen carrier features ~100% CH₄ conversions and a syngas yield of 12.5 mol·kg⁻¹ in the COG conversion step. In regard to the H₂O splitting step, the H₂ yield (3.3 mol·kg⁻¹) is 200% higher than that of LaFeO₃, with the hydrogen purity closed to 100%. Furthermore, after 50 successive redox cycles, no decrease in the syngas yield in COG conversion step and H₂ yields in H₂O splitting step is observed, indicating excellent stability in redox cycles. As revealed by the experimental investigations and DFT calculations, the superior performance of LaNi_{0.07}Fe_{0.93}O_{3-λ} in COG conversion step is driven by the catalytic role on Ni species for adsorbing and activating methane. In addition, the Ni species in the reduced LaNi_{0.07}Fe_{0.93}O_{3-λ} sample can also promote the conversion of H₂O to H₂ at relatively low temperatures. The basic understanding of the catalytic sites of the doped perovskite oxygen carriers may explore a reasonable method for design advanced materials in chemical looping technology.

CRedit authorship contribution statement

Yanhui Long: Formal analysis, Data curation, writing original draft, performed the catalyst preparation, catalytic tests, data analysis and wrote this paper, designed the study and wrote the paper. **Kun Yang:** Formal analysis, Data curation. **Zhenhua Gu:** Writing - original draft, conducted DFT calculations and wrote the computational section. **Shen Lin:** conducted the FTIR experiments. **Danyang Li:** performed the in situ XPS experiment. **Zhu Xing:** performed DFT calculations. **Hua Wang:** Data curation. **Kongzhai Li:** Writing - original draft, designed the study and wrote the paper. All authors discussed the results and commented on the manuscript.

Declaration of Competing Interest

The authors declare that they have no known competing financial interests or personal relationships that could have appeared to influence the work reported in this paper.

Acknowledgements

The National Key R&D Program of China (2018YFB0605401), National Natural Science Foundation of China (No. 51774159) and the Qinglan Project of Kunming University of Science and Technology supported this work.

Appendix A. Supporting information

Supplementary data associated with this article can be found in the online version at [doi:10.1016/j.apcatb.2021.120778](https://doi.org/10.1016/j.apcatb.2021.120778).

References

- [1] M. Luo, Y. Yi, S. Wang, Z. Wang, M. Du, J. Pan, Q. Wang, Review of hydrogen production using chemical-looping technology, *Renew. Sustain. Energy Rev.* 81 (2018) 3186–3214.
- [2] J.M. Thomas, P.P. Edwards, P.J. Dobson, G.P. Owen, Decarbonising energy: the developing international activity in hydrogen technologies and fuel cells, *J. Energy Chem.* 51 (2020) 405–415.
- [3] N. Sazali, Emerging technologies by hydrogen: a review, *Int. J. Hydrog. Energy* 45 (2020) 18753–18771.
- [4] X. Zhu, Q. Imtiaz, F. Donat, C.R. Müller, F. Li, Chemical looping beyond combustion – a perspective, *Energy Environ. Sci.* 13 (2020) 772–804.
- [5] Q. Yi, M.-H. Gong, Y. Huang, J. Feng, Y.-H. Hao, J.-L. Zhang, W.-Y. Li, Process development of coke oven gas to methanol integrated with CO₂ recycle for satisfactory techno-economic performance, *Energy* 112 (2016) 618–628.
- [6] R. Razaq, C. Li, S. Zhang, Coke oven gas: availability, properties, purification, and utilization in China, *Fuel* 113 (2013) 287–299.
- [7] Z. Li, Q. Yi, Y. Zhang, H. Zhou, Y. Zhao, Y. Huang, D. Gao, Y. Hao, Numerical study and design strategy for a low emission coke oven system using oxy-fuel combustion of coke oven gas, *J. Clean. Prod.* 252 (2020), 119656.
- [8] S. Han, S. Kim, Y.T. Kim, G. Kwak, J. Kim, Optimization-based assessment framework for carbon utilization strategies: energy production from coke oven gas, *Energy Convers. Manag.* 187 (2019) 1–14.
- [9] S.C.J. Van Acht, C. Laycock, S.J.W. Carr, J. Maddy, A.J. Guwy, G. Lloyd, L.F.J. M. Raymakers, Simulation of integrated novel PSA/EHP/C process for high-pressure hydrogen recovery from Coke Oven Gas, *Int. J. Hydrog. Energy* 45 (2020) 15196–15212.
- [10] A.D. Hernandez, N. Kaisalo, P. Simell, M. Scarsella, Effect of H₂S and thiophene on the steam reforming activity of nickel and rhodium catalysts in a simulated coke oven gas stream, *Appl. Catal. B: Environ.* 258 (2019), 117977.
- [11] B. Zhang, Y. Chen, B. Kang, J. Qian, X. Chuai, R. Peng, Z. Li, F. Guo, W. Yan, J. Zhang, Hydrogen production via steam reforming of coke oven gas enhanced by steel slag-derived CaO, *Int. J. Hydrog. Energy* 45 (2020) 13231–13244.
- [12] J.M. Bermúdez, A. Arenillas, R. Luque, J.A. Menéndez, An overview of novel technologies to valorise coke oven gas surplus, *Fuel Process. Technol.* 110 (2013) 150–159.
- [13] H.W. Cheng, X.G. Lu, D.H. Hu, Y.W. Zhang, W.Z. Ding, Q.D. Zhong, Improving performance of BaCo_{0.7}Fe_{0.2}Nb_{0.1}O_{3-δ} ceramic membrane by a surface-coating layer for partial oxidation of coke oven gas, *Adv. Mater. Res.* 154–155 (2010) 877–881.
- [14] H. Xie, Q. Yu, H. Lu, L. Ji, H. Chen, Q. Qin, Selection and preparation of CO₂ sorbent for sorption-enhanced steam reforming process of raw coke oven gas, *Environ. Prog. Sustain. Energy* 38 (2019) 89–97.
- [15] H.-M. Kim, B.-J. Kim, W.-J. Jang, J.-O. Shim, K.-W. Jeon, H.-S. Na, Y.-L. Lee, B.-H. Jeon, H.-S. Roh, Effect of support materials and Ni loading on catalytic performance for carbon dioxide reforming of coke oven gas, *Int. J. Hydrog. Energy* 44 (2019) 8233–8242.
- [16] Y. Zhang, T. Liu, J. Zhang, C. Wu, X. Lu, W. Ding, Induction brazing BaCo_{0.7}Fe_{0.2}Nb_{0.1}O_{3-δ} membrane tubes to steel supports with Ag-based filler in air, *J. Membr. Sci.* 533 (2017) 19–27.
- [17] W. Yao, H. Cheng, H. Zhao, X. Lu, X. Zou, S. Li, C. Li, Synthesis, oxygen permeability, and structural stability of BaCo_{0.7}Fe_{0.3-δ}Zr_xO_{3-δ} ceramic membranes, *J. Membr. Sci.* 504 (2016) 251–262.
- [18] Y. Chen, R. Peng, Y. Xiao, B. Zhang, J. Zhang, Efficient hydrogen production from coke oven gas by sorption-enhanced steam reforming in a membrane-assisted fluidized bed reactor, *Energy Fuels* 33 (2019) 11420–11438.
- [19] Y. Long, K. Li, Z. Gu, X. Zhu, Y. Wei, C. Lu, S. Lin, K. Yang, X. Cheng, D. Tian, F. He, H. Wang, Ce-Fe-Zr-O/MgO coated monolithic oxygen carriers for chemical looping reforming of methane to co-produce syngas and H₂, *Chem. Eng. J.* 388 (2020), 124190.
- [20] S. Lin, Z. Gu, X. Zhu, Y. Wei, Y. Long, K. Yang, F. He, H. Wang, K. Li, Synergy of red mud oxygen carrier with MgO and NiO for enhanced chemical-looping combustion, *Energy* 197 (2020), 117202.
- [21] D. Li, R. Xu, Z. Gu, X. Zhu, S. Qing, K. Li, Chemical-looping conversion of methane: a review, *Energy Technol.* 8 (2019), 1900925.
- [22] L. Zeng, Z. Cheng, J.A. Fan, L.-S. Fan, J. Gong, Metal oxide redox chemistry for chemical looping processes, *Nat. Rev. Chem.* 2 (2018) 349–364.
- [23] D. Li, R. Xu, X. Li, Z. Li, X. Zhu, K. Li, Chemical looping conversion of gaseous and liquid fuels for chemical production: a review, *Energy Fuels* 34 (2020) 5381–5413.
- [24] S. Ma, M. Li, G. Wang, L. Zhang, S. Chen, Z. Sun, J. Hu, M. Zhu, W. Xiang, Effects of Zr doping on Fe₂O₃/CeO₂ oxygen carrier in chemical looping hydrogen generation, *Chem. Eng. J.* 346 (2018) 712–725.
- [25] X. Zhang, C. Pei, X. Chang, S. Chen, R. Liu, Z.J. Zhao, R. Mu, J. Gong, FeO₆ octahedral distortion activates lattice oxygen in perovskite ferrite for methane partial oxidation coupled with CO₂ splitting, *J. Am. Chem. Soc.* 142 (2020) 11540–11549.
- [26] E. Ksepko, R.V. Siriwardane, H. Tian, T. Simonyi, M. Sciazko, Effect of H₂S on chemical looping combustion of coal-derived synthesis gas over Fe–Mn oxides supported on sepiolite, ZrO₂, and Al₂O₃, *Energy Fuels* 26 (2012) 2461–2472.
- [27] F. García-Labiano, L.F. de Diego, P. Gayán, A. Abad, A. Cabello, J. Adánez, G. Sprachmann, Energy exploitation of acid gas with high H₂S content by means of a chemical looping combustion system, *Appl. Energy* 136 (2014) 242–249.
- [28] L. Wang, X. Feng, L. Shen, S. Jiang, H. Gu, Carbon and sulfur conversion of petroleum coke in the chemical looping gasification process, *Energy* 179 (2019) 1205–1216.
- [29] X. Zhu, K. Li, L. Neal, F. Li, Perovskites as geo-inspired oxygen storage materials for chemical looping and three-way catalysis: a perspective, *ACS Catal.* 8 (2018) 8213–8236.
- [30] M. Tang, X. Long, M. Fan, Progress in oxygen carrier development of methane-based chemical-looping reforming: a review, *Appl. Energy* 151 (2015) 143–156.
- [31] Y. Zheng, K. Li, H. Wang, D. Tian, Y. Wang, X. Zhu, Y. Wei, M. Zheng, Y. Luo, Designed oxygen carriers from macroporous LaFeO₃ supported CeO₂ for chemical-looping reforming of methane, *Appl. Catal. B: Environ.* 202 (2017) 51–63.
- [32] O. Mihai, D. Chen, A. Holmen, Catalytic consequence of oxygen of lanthanum ferrite perovskite in chemical looping reforming of methane, *Ind. Eng. Chem. Res.* 50 (2011) 2613–2621.
- [33] X. Dai, J. Cheng, Z. Li, M. Liu, Y. Ma, X. Zhang, Reduction kinetics of lanthanum ferrite perovskite for the production of synthesis gas by chemical-looping methane reforming, *Chem. Eng. Sci.* 153 (2016) 236–245.
- [34] X.P. Dai, R.J. Li, C.C. Yu, Z.P. Hao, Unsteady-state direct partial oxidation of methane to synthesis gas in a fixed-bed reactor using AFeO₃ (A = La, Nd, Eu) perovskite-type oxides as oxygen storage, *J. Phys. Chem. B* 110 (2006) 22525–22531.
- [35] K. Zhao, F. He, Z. Huang, A. Zheng, H. Li, Z. Zhao, Three-dimensionally ordered macroporous LaFeO₃ perovskites for chemical-looping steam reforming of methane, *Int. J. Hydrog. Energy* 39 (2014) 3243–3252.
- [36] Y. Shen, K. Zhao, F. He, H. Li, The structure-reactivity relationships of using three-dimensionally ordered macroporous LaFe_{1-x}Ni_xO₃ perovskites for chemical-looping steam methane reforming, *J. Energy Inst.* 92 (2019) 239–246.
- [37] M. Lee, H.S. Lim, Y. Kim, J.W. Lee, Enhancement of highly-concentrated hydrogen productivity in chemical looping steam methane reforming using Fe-substituted LaCoO₃, *Energy Convers. Manag.* 207 (2020), 112507.
- [38] H. Arai, T. Yamada, K. Eguchi, T. Seiyama, Catalytic combustion of methane over various Perovskite-type oxides, *Appl. Catal.* 26 (1986) 265–276.
- [39] K. Zhao, F. He, Z. Huang, G. Wei, A. Zheng, H. Li, Z. Zhao, Perovskite-type oxides LaFe_{1-x}Co_xO₃ for chemical looping steam methane reforming to syngas and hydrogen co-production, *Appl. Energy* 168 (2016) 193–203.
- [40] Y. Wang, Y. Zheng, Y. Wang, H. Wang, X. Zhu, Y. Wei, Y. Wang, L. Jiang, Z. Yang, K. Li, Evaluation of Fe substitution in perovskite LaMnO₃ for the production of high purity syngas and hydrogen, *J. Power Sources* 449 (2020), 227505.
- [41] F.H. Taylor, J. Buckeridge, C.R.A. Catlow, Screening divalent metals for A- and B-site dopants in LaFeO₃, *Chem. Mater.* 29 (2017) 8147–8157.
- [42] D. Sastre, D.P. Serrano, P. Pizarro, J.M. Coronado, Chemical insights on the activity of La_{1-x}Sr_xFeO₃ perovskites for chemical looping reforming of methane coupled with CO₂-splitting, *J. CO₂ Util.* 31 (2019) 16–26.
- [43] C. Ruan, Z.-Q. Huang, J. Lin, L. Li, X. Liu, M. Tian, C. Huang, C.-R. Chang, J. Li, X. Wang, Synergy of the catalytic activation on Ni and the CeO₂-TiO₂/Ce₂Ti₂O₇ stoichiometric redox cycle for dramatically enhanced solar fuel production, *Energy Environ. Sci.* 12 (2019) 767–779.
- [44] S. Chen, L. Zeng, H. Tian, X. Li, J. Gong, Enhanced lattice oxygen reactivity over Ni-modified WO₃-based redox catalysts for chemical looping partial oxidation of methane, *ACS Catal.* 7 (2017) 3548–3559.
- [45] S.-K. Otto, K. Kousi, D. Neagu, L. Bekris, I. Metcalfe, Exsolved Ni nanoparticles acting as oxygen storage reservoirs and active sites for redox CH₄ conversion, *ACS Appl. Energy Mater.* 2 (2019) 7288–7298.
- [46] L. Nalbandian, A. Evdou, V. Zaspalis, La_{1-x}Sr_xMyFe_{1-y}O_{3-δ} perovskites as oxygen-carrier materials for chemical-looping reforming, *Int. J. Hydrog. Energy* 36 (2011) 6657–6670.
- [47] J. Yan, W. Liu, R. Sun, S. Jiang, S. Wang, L. Shen, Chemical looping catalytic gasification of biomass over active LaNi_{0.5}Fe_{0.5}O₃ perovskites as functional oxygen carriers, *Chin. J. Chem. Eng.* (2020).
- [48] J.P. Perdew, K. Burke, M. Ernzerhof, Generalized gradient approximation made simple [Phys. Rev. Lett. 77, 3865 (1996)], *Phys. Rev. Lett.* (1997).
- [49] K. Yang, Z. Gu, Y. Long, S. Lin, C. Lu, X. Zhu, H. Wang, K. Li, Hydrogenation production via chemical looping reforming of coke oven gas, *Green. Energy Environ.* 6 (2020) 678–692.
- [50] S. Zhao, X. Wu, C.K. Russell, M. Dyar, E.C. Sklute, S. Toan, M. Fan, L. Duan, W. Xiang, Synergistic enhancement of chemical looping-based CO₂ splitting with biomass cascade utilization using cyclic stabilized Ca₂Fe₂O₅ aerogel, *J. Mater. Chem. A* 7 (2019).
- [51] Y. Zhu, R. Liu, X. Sun, X. Ma, X. Wang, H. Tian, Metal modified hexaaluminates for syngas generation and CO₂ utilization via chemical looping, *Int. J. Hydrog. Energy* 44 (2019) 10218–10231.

- [52] L. Zhuang, L. Ge, Y. Yang, M. Li, Y. Jia, X. Yao, Z. Zhu, Ultrathin iron-cobalt oxide nanosheets with abundant oxygen vacancies for the oxygen evolution reaction, *Adv. Mater.* 29 (2017).
- [53] D. Li, K. Li, R. Xu, X. Zhu, Y. Wei, D. Tian, X. Cheng, H. Wang, Enhanced CH₄ and CO oxidation over Ce_{1-x}Fe_xO_{2-delta} hybrid catalysts by tuning the lattice distortion and the state of surface iron species, *ACS Appl. Mater. Interfaces* 11 (2019) 19227–19241.
- [54] Z. Huang, F. He, Y. Feng, K. Zhao, A. Zheng, S. Chang, G. Wei, Z. Zhao, H. Li, Biomass char direct chemical looping gasification using NiO-modified iron ore as an oxygen carrier, *Energy Fuels* 28 (2013) 183–191.
- [55] Z. Cheng, L. Qin, M. Guo, J. Fan D., L., Methane adsorption and dissociation on iron oxide oxygen carriers: the role of oxygen vacancies, *Phys. Chem. Chem. Phys. Camb. R. Soc. Chem.* 18 (2016) 16423–16435.
- [56] M.B. Lee, Q.Y. Yang, S.T. Ceyer, Dynamics of the activated dissociative chemisorption of CH₄ and implication for the pressure gap in catalysis: a molecular beam–high resolution electron energy loss study, *J. Chem. Phys.* 87 (1987) 2724–2741.
- [57] R.C. Egeberg, S. Ullmann, I. Alstrup, C.B. Mullins, I. Chorkendorff, Dissociation of CH₄ on Ni(111) and Ru(0001), 497 (2002) 0–193.
- [58] K. Zhao, J. Chen, H. Li, A. Zheng, F. He, Effects of co-substitution on the reactivity of double perovskite oxides LaSrFe_{2-x}Co_xO₆ for the chemical-looping steam methane reforming, *J. Energy Inst.* (2018). S1743967118301314.
- [59] A. Kubacka, R. Si, P. Michorczyk, A. Martínez-Arias, W. Xu, J.C. Hanson, J. A. Rodriguez, M. Fernández-García, Tungsten as an interface agent leading to highly active and stable Copper-Ceria water gas shift catalyst, *Appl. Catal. B Environ.* 132 (2013) 423–432.
- [60] R.C. Stehle, M.M. Bobek, R. Hooper, D.W. Hahn, Oxidation reaction kinetics for the steam-iron process in support of hydrogen production, *Int. J. Hydrog. Energy* 36 (2011) 15125–15135.
- [61] J. Carrasco, D. Lopez-Duran, Z. Liu, T. Duchon, J. Evans, S.D. Senanayake, E. J. Crumlin, V. Matolin, J.A. Rodríguez, M.V. Ganduglia-Pirovano, In situ and theoretical studies for the dissociation of water on an active Ni/CeO₂ catalyst: importance of strong metal-support interactions for the cleavage of O-H bonds, *Angew. Chem. Int Ed. Engl.* 54 (2015) 3917–3921.